Conference Report

The High-Density Symmetry Energy in Heavy-Ion Collisions and Compact Stars

Hermann Wolter [ID]

Faculty of Physics, University of Munich, 85748 Garching, Germany; hermann.wolter@lmu.de;
Tel.: +49-179-917-8954

check for
updates

Abstract: High-density nuclear symmetry energy is of crucial importance in astrophysics. Information on such energy has been obtained from mass–radius determinations of neutron stars (NSs), and in the future NS mergers will increasingly contribute. In the laboratory, the symmetry energy can be studied in heavy-ion collisions (HICs) at different incident energies over a large range, from very low to several times higher saturation density. Transport theory is necessary to extract the symmetry energy from the typically non-equilibrated nuclear collisions. In this contribution, we first review the transport approaches, their differences, and recent studies of their reliability. We then discuss several prominent observables, which have been used to determine the symmetry energy at high density: collective flow, light cluster emission, and particle production. It is finally argued that the results of the symmetry energy from microscopic many-body calculations, nuclear structure, nuclear reactions, and astrophysics begin to converge but still need considerable improvements in terms of accuracy.

1. Introduction

The nuclear equation of state (EoS) specifies the energy density of nuclear matter without Coulomb energy as a function of density, temperature, and asymmetry. For zero temperature, it is usually written in the lowest order in asymmetry as $E(\rho, \delta) = E_0(\rho) + E_{sym}(\rho)\delta^2$, where $\delta = (\rho_n - \rho_p)/\rho$ and ρ_n, ρ_p, and ρ are the neutron, proton, and total densities, respectively. The energy density of symmetric nuclear matter E_0 has been extensively investigated in heavy-ion collisions (HICs) in the past, and a consensus has been reached: that it is rather soft, that is, rises less than linearly with density, and is also momentum dependent [1,2]. The nuclear symmetry energy $E_{sym}(\rho)$ is less well understood. Studies with HICs at energies below about 400 MeV have constrained it fairly well around and below saturation density $\rho_0 \approx 0.16$ fm/c [3]. However, the high-density behavior is still a matter of debate. Microscopic many-body calculations still diverge considerably at higher densities. The reasons are seen in the uncertainty of three-body forces and of short-range isovector correlations and in the question of the strangeness content. The symmetry energy is often represented as an expansion around saturation density as $E_{sym}(\rho) = S_0 + \frac{L}{3}\frac{\rho - \rho_0}{\rho_0} + \frac{K_{sym}}{18}(\frac{\rho - \rho_0}{\rho_0})^2$, where S_0 is the value and L and K_{sym} proportional to the slope and curvature, respectively, of the symmetry energy at saturation. L has been determined to be in the range of 50 to 100 MeV [3] and is a measure of the stiffness of the symmetry energy.

On the other hand, the nuclear symmetry energy is a crucial input for the understanding of astrophysical objects. The structure of neutron stars (NSs) and the explodability of core-collapse supernovae (CCSNe) depend critically on the properties of neutron-rich nuclear matter and thus on the symmetry energy. Astrophysical observations have yielded important constraints on the nuclear symmetry energy. The Tolman–Openheimer–Volkov equation relates the symmetry energy directly to

the mass–radius relation of NSs. The observation of NSs with masses of around 2 solar masses already excludes symmetry energies that are too soft [4]. Radii are difficult to measure, as they depend on the interpretation of γ- or X-ray emission and are even more difficult to obtain simultaneously with masses. However, Bayesian analysis methods already also set limits here [5,6]. The satellite experiment Neutron star Interior Composition Explorer (NICER) should provide more and better data.

The very recent discovery of the gravitational wave event GW170817 from a NS merger [7], together with the observation of a short gamma-ray burst (GRB) [8,9] and the optical afterglow, promises further important insights into high-density symmetry energy. In addition to determining the masses of the merging NSs, it was possible to obtain limits on their tidal deformabilities, which are also directly given by the EoS, similarly to the mass–radius relation of NSs [10]. Figure 1 shows an example of the results of interpretations of the NS merger [11,12]. The mass–radius relation for a number of models for the EoS is shown together with the constraints originating from the observation of 2 solar mass NSs, as well as from the limits of the tidal deformabilities of the GW170817 event [13]. It is seen that these constraints together already exclude several models for the EoS. If the possibility of a quark phase in the interior of NSs is considered, the constraints become more complex [14]. Further observations of NS mergers will provide more information in the future.
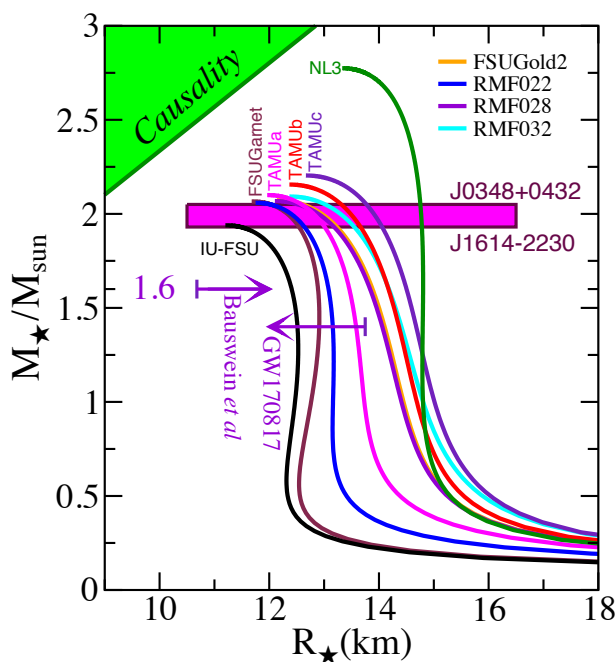

Figure 1. (Color on-line) Mass–radius relation of neutron stars (NSs) predicted for different relativistic mean-field (RMF) models identified in the legend. Shown also are the masses of two heavy NSs and the constraints following from the tidal deformability of the GW event. Figure taken from [11] with permission.

The EoS can also be investigated in terrestrial laboratories in HICs. In energetic collisions, densities of up to several times the saturation density can be reached, similar to those that are thought to exist in NSs. In HICs, one has the possibility to scan the density in certain ranges via the incident energy and colliding masses and the asymmetry by the choice of the collision system. The latter is limited by the asymmetries of available projectiles and targets but is being extended by the use of exotic beams. However, the high-density phase only exists for the short time span of the collision in the order of 1 to 100 fm/c, depending on the energy. In order to draw conclusions from the final asymptotic observables to the properties of the dense medium, the evolution of the collision has to be described in detail. This is achieved by various transport descriptions. As the system in these collisions is out of equilibrium for most of the time, transport also takes into account the non-equilibrium nature. Hydrodynamical

treatments, which assume a local equilibrium, and statistical treatments, which assume a global equilibrium, are often not adequate, at least not for the whole process. On the other hand, transport descriptions are complex, and the necessary approximations, the implementations, and the accuracy are issues that also have to be discussed.

This contribution aims to review the issues, the problems, and some of the results of the study of high-density symmetry energy with emphasis on HICs. Thus we first discuss the transport theories and then give some examples of observables that have been used to constrain the symmetry energies. It is beyond the scope here to discuss in more detail than the above the constraints on the symmetry energy from NS observations. A good collection of articles regarding this can be found in the recent special volume on symmetry energy, published by B.A. Li et al. in [2]. Finally, we summarize the present status of these studies on symmetry energy.

2. Theoretical Considerations

2.1. Overview of Transport Theories

Transport theory is necessary to draw conclusions on the EoS from HIC experiments to account for the non-equilibrium nature of the process. Practical transport approaches are derived from non-equilibrium many-body physics by a chain of approximations [15,16]. One usually starts from the Martin–Schwinger real-time Green function formalism, which by a folded time path with forward and backward branches takes into account the time-reversal asymmetry. The hierarchy of many-body densities is truncated by the factorization of the two-body density and by introducing single-particle self-energies. One arrives at the Kadanoff–Baym theory for the non-local densities and self-energies. With a Wigner transform, this is cast into an equation in phase space $\{\vec{r}, \vec{p}\}$. A gradient approximation in the first order in $\hbar$ leads to a semiclassical description, where a quantity $f(\vec{r}, \vec{p}; t)$ can be interpreted as the phase-space probability. At this stage, there are still two independent Green functions, which can be transformed into the above phase-space probability and a spectral function for the off-shell particles. In the quasi-particle approximation, the spectral function is taken to be on-shell in terms of effective momenta and masses. With these approximations, one arrives at an equation of the Boltzmann–Vlasov type for the evolution of the phase-space probability $f(\vec{r}, \vec{p}; t)$ under the influence of a self-consistent mean field $U[f]$ and of two-body collisions as the dissipative mechanism, which non-relativistically reads

$$\frac{\partial f_1}{\partial t} + \frac{\vec{p}}{m} \nabla_{\vec{r}} f_1 - \nabla_{\vec{r}} U \nabla_{\vec{p}} f_1 = \tag{1}$$
$$(\frac{2\pi}{m})^3 \int d\vec{p}_2 d\vec{p}_3 d\vec{p}_4 |\vec{v}_1 - \vec{v}_2| \sigma_{NN}(\Omega_{12}) \delta(\vec{p}_1 + \vec{p}_2 - \vec{p}_3 - \vec{p}_3)(f_3 f_4 \bar{f}_1 \bar{f}_2 - f_1 f_2 \bar{f}_3 \bar{f}_4).$$

Here $f_i \equiv f(\vec{r}, \vec{p}_i; t)$ and $\bar{f}_i = (1 - f_i)$ are the blocking factors, which assure the Pauli principle for the final state of a collision, and which are the essential quantum ingredient in this equation apart from the initialization. The v_i are velocities, and $\sigma_{NN}(\Omega)$ is the in-medium nucleon–nucleon (NN) cross-section. The potential $U[f]$ and the cross-section are either derived from a nuclear energy density functional $E[f]$ or are parametrized. The Coulomb interaction is included separately. If the energy functional explicitly depends on f, then the potential can be momentum dependent, which adds another term to the left-hand side of the transport equation. The physical components of the equation, namely, the potential and in-medium cross-sections, are not independent, but are connected by an approximation scheme for the self-energies. An obvious choice is the Brückner scheme for the effective in-medium interaction, used in a local-density approximation. This has either been used directly [17] or in parametrized Yukawa-like form with meson–nucleon couplings, which depend on the density and may in addition depend on the energy [18,19]. If particle production, for example, of pions and Δ resonances, is to be considered, additional physics input is needed: inelastic

cross-sections, potentials of the new particles, their cross-sections, and, possibly, mass distributions of unstable particles, simulating the off-shell effects.

The temperature T does not enter explicitly into the transport equation but rather into the distribution function, which may or may not be well represented by an equilibrium distribution, which could be characterized by a temperature. If the interaction is specified by an energy density functional, then these effects are implicitly included. The same functional is then evaluated for a ground-state distribution function to obtain the EoS and the symmetry energy at zero temperature.

Equation (1) is often referred to as the Boltzmann–Uehling–Uhlenbeck (BUU) equation but is also known by other names. It is a complex non-linear integro-differential equation, which is usually solved by the test particle (TP) method, where the distribution function is represented in terms of finite elements, TPs, as

$$f(\vec{r}, \vec{p}; t) = \frac{1}{N_{TP}} \sum_{i=1}^{AN_{TP}} g(\vec{r} - \vec{r}_i(t)) \, \tilde{g}(\vec{p} - \vec{p}_i(t)). \tag{2}$$

Here N_{TP} is the number of TPs per nucleon, $\vec{r}_i$ and $\vec{p}_i$ are the time-dependent coordinates and momenta of the TPs, and g and $\tilde{g}$ are the shape functions in coordinate and momentum space (e.g., δ-functions or Gaussians), respectively. Upon inserting this ansatz into the left-hand side of Equation (2), Hamiltonian equations of motion for the TPs are obtained, $\frac{d\vec{r}_i}{dt} = \vec{p}_i$ and $\frac{d\vec{p}_i}{dt} = -\vec{\nabla}_{r_i} U$. The collision term is simulated stochastically, by performing TP collisions with a probability depending on the cross-section and obeying the Pauli principle for the final state according to blocking factors $\bar{f}_i = (1 - f_i)$.

A second family of transport approaches is the quantum molecular dynamics (QMD) model, in which the evolution of the collision is formulated in terms of the evolution of the coordinates $R_i(t)$ and momenta $P_i(t)$ of the individual nucleons, similarly to as in classical molecular dynamics, but with particles of finite width representing minimum nucleon wave packets, with the width usually assumed to be constant. These move under the influence of NN forces. The method can also be viewed as being derived from the time-dependent Hartree (TDH) method with a product trial wave-function of single-particle states in Gaussian form. One obtains equations of motion of the same form as in BUU in this case for the coordinates of the wave packets. There is also a version of anti-symmetrized molecular dynamics (AMD) [20], which takes into account the anti-symmetrization of the wave packets. The equations of motion become non-local but are of similar type. Additionally, in QMD and AMD, a stochastic two-body collision term is introduced and treated in very much the same way as in BUU, but now for nucleons and the full NN cross-section. There are also relativistic formulations for both approaches using relativistic density functionals. A review of the BUU method is given in [21], while the QMD method is reviewed in [22].

2.2. Fluctuations

The main difference between the two approaches lies in the number of fluctuations and correlations in the representation of the phase-space distribution. In the BUU approach, the phase-space distribution function is seen as a smooth function of coordinates and momenta and can be increasingly better approximated by increasing the number of TPs. In the limit of $N_{TP} \to \infty$, the TP method provides an exact solution of the BUU equation, which is strictly deterministic and has no fluctuations. However, fluctuations are a necessary companion of dissipative dynamics, as expressed by the dissipation–fluctuation theorem. In practice, they are important in the expansion phase of a HIC, which often proceeds through mechanically unstable conditions and may lead to fragmentation of the residual nuclei. If such phenomena are to be described, one has to add a fluctuation term to the equation, which leads to the Boltzmann–Langevin equation. Approximate treatments of fluctuations in HICs have been implemented in [23–26]. In practice, N_{TP} is finite, in the order of 50 to 100 depending on the assumed shape of the TP, which leads to numerical fluctuations. In early treatments, these have been gauged to reproduce the unstable properties of the medium. In QMD,

fluctuations are present because of the intrinsically finite number of wave packets in the representation of the phase space. The fluctuations are smoothed and regulated by the choice of the width parameter of the wave packets. In addition, classical correlations are present if explicit two-body interactions are used. QMD can be seen as an event generator solving the time evolution of different events independently. Event-by-event fluctuations are not suppressed by increasing the number of events.

The results of simulations with the two methods are thus expected to be similar, although not necessarily identical, as far as one-body observables are concerned. Larger differences are expected for observables depending on fluctuations and correlations, such as the production of clusters and intermediate-mass fragments. Generally, the description of observables going beyond the mean-field level is a question under active discussion in transport theory. In the experiment, copious numbers of light clusters and fragments were observed in HICs, particularly at lower energies.

2.3. Code Comparison

In addition to these more fundamental differences between transport approaches, there are also differences that are caused by different implementations of the highly complex transport theories. Analyses of experimental data with seemingly similar physics input have led to rather different conclusions. The analyses of the FOPI π^-/π^+ ratios, as discussed below, represent an example. In order to reach a better understanding of possible reasons, a code-comparison project was undertaken. In a first comparison, results for standard Au+Au collisions at 100 and 400 AMeV incident energies with identical physics input were compared [27]. Eighteen commonly used transport codes, of both BUU and QMD type, participated. Comparisons of the stability of the initialized configuration; of the collision rates and the effectiveness of Pauli blocking; and of observables, such as the longitudinal and transverse flow, were discussed. The results for the flow parameter, that is, for the slope of the transverse flow at midrapidity, are shown in Figure 2 for the different codes. We are more interested here in the qualitative behavior of the different codes. It would go beyond the scope to identify the different codes and their properties in detail; one should refer rather to [27]. While there is a general agreement, quantitatively the differences were found to depend on the incident energy and amounted to approximately 30% at 100 MeV/nucleon and 15% at 400 MeV/nucleon, respectively.
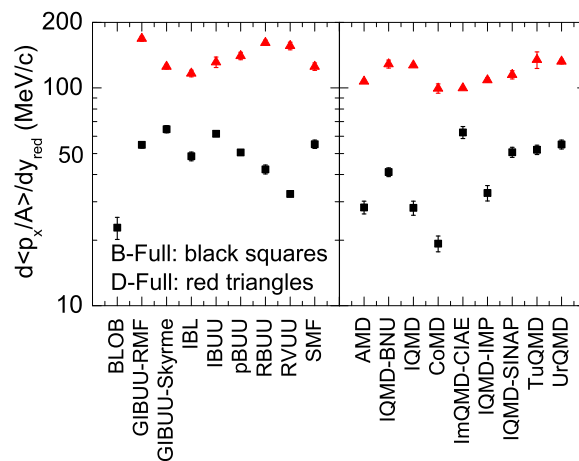

Figure 2. (Color on-line) Comparison of flow parameters (transverse momentum at midrapidity) in Au+Au collisions at 100 AMeV (square (black) symbols) and 400 AMeV (triangular (red) symbols) for codes of Boltzmann–Uehling–Uhlenbeck (BUU) type (left) and quantum molecular dynamics (QMD) type (right). For the identification of the different codes, see [27], from where this figure is taken.

In order to better understand these still appreciable differences, this was followed up by a comparison of calculations in a box with periodic boundary conditions, which approximates a calculation in infinite nuclear matter. The advantages of box calculations are that common initial

conditions of a given density and temperature are easier to achieve, that the different ingredients of the transport codes can be tested separately, and that the results can be compared in many cases to exact limits. A first comparison of this kind investigated the treatment of the collision integral by switching off the mean field, without and with including the Pauli blocking, that is, by comparing Cascade calculations [28]. Without the Pauli blocking, the codes agreed to within a few percent among each other and with the exact limits, and the remaining small differences could be understood in most cases. Including the Pauli blocking, there were considerable differences. The collision rates for initializations of normal density and temperature $T = 5$ MeV for the different codes are shown in Figure 3 and compared to the exact limit, represented there by the line labeled CBOP2T5. Again, we do not discuss the different codes in detai; this is done in [28]. The results are shown for the first time step, for which the momentum distributions were still identical, and were time-averaged over the evolution, during which the momentum distribution changed in different ways for the different codes. These differences are seen not to be very important relative to the considerable differences seen regarding the exact limit. There are systematic differences between BUU and QMD and also between codes of the same kind. The main reason for the differences was found to be from fluctuations when calculating the occupation probability in the final phase-space cell of the collision partners, which led to differences in the Pauli blocking. These fluctuations, and their differences in BUU and QMD approaches, are discussed above. The consequence of the larger fluctuations in QMD codes was seen in systematically higher collision rates. On the other hand, the proper treatment of fluctuations in transport codes is still debated. The box comparisons are presently continued for the mean-field propagation and for pion production. It is anticipated that these comparisons can provide benchmark calculations against which existing and new transport codes can be compared.
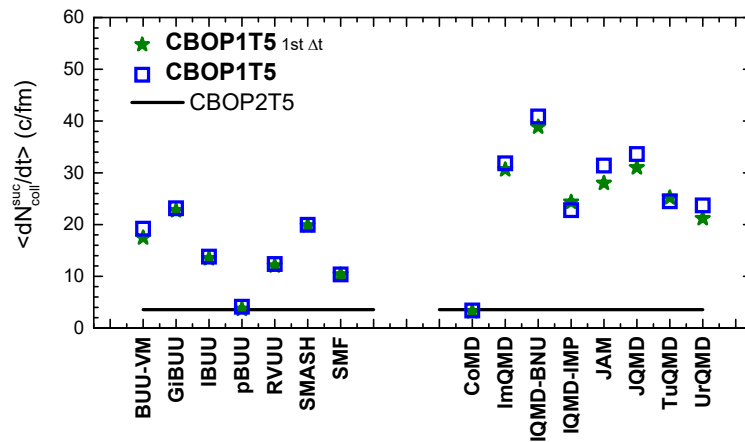

Figure 3. (Color on-line) Comparison of collision rates in box calculations at normal density and temperature $T = 5$ MeV (denoted as CBOP1T5) for different Boltzmann–Uehling–Uhlenbeck (BUU)-type (**left**) and quantum molecular dynamics (QMD)-type (**right**) codes. Star symbols give the result for the first time step; square symbols give time-averaged rates. They are compared to a numerical, essentially exact, result for this case (solid line, denoted as CBOP2T5). For the identification of different codes, see [28], from where this figure is taken.

3. Symmetry Energy in Heavy-Ion Collisions

3.1. Overview

In intermediate-energy HICs, dense and hot matter is formed for very short time periods in the order of 10^{-22} fm/c. The connection of these conditions to the asymptotic observables is provided by transport approaches as discussed above. Nuclear matter in HICs is only moderately asymmetric with asymmetries $\delta < 0.2$. Thus in HICs, both the EoS of symmetric nuclear matter E_0 and the symmetry energy E_{sym} are involved, with the symmetric matter giving the greatest

contribution. In the past, the emphasis for HICs was put on the investigation of the symmetric EoS. It is thought that this has been fairly well determined by a variety of probes, mainly connected to collective phenomena [1] and to K-meson ratios [29]. The sensitivity to the symmetry energy part of the EoS can be increased by focusing on ratios or differences of observables for isospin partners, such as, for example, protons and neutrons or positively and negatively charged pions, hoping that the still-existent uncertainties in the isoscalar part of the EoS cancel out to a large extent.

The densities reached in HICs depend on the incident energy, on the system masses, and on the impact parameter of the collision. For peripheral collisions, the spectator–participant model has been useful, as it separates the warmly heated spectators of initially normal density from the strongly excited fireball, which on the other hand is observed in central collisions of similar-size ions. For energies of up to a few hundred MeV per nucleon in central collisions, densities about 20–30% in excess of saturation density are reached. In this regime, the interest is particularly on the decay and subsequent fragmentation, which contain rich information on the symmetry energy at densities below saturation in the isospin sharing of the fragments. Particularly, the value and the slope of the symmetry energy at saturation energy are extracted in these studies [3,30].

In relativistic collisions, up to several GeV per nucleon densities of up to 2–3 ρ_0 are reached. The collective motion of the final particles represents direct evidence of the symmetry energy, because the neutron–proton differences are directly driven by the isospin-dependent part of the mean field and thus by the symmetry energy. Additionally, nucleons and light clusters are emitted early in the collision, and the ratios of this pre-equilibrium emission gives complementary information on the symmetry energy at high density. Finally, in energetic collisions, mesons are produced in increasing multiplicities. The production of isospin partners depends on the asymmetry of the matter in which they are produced, and thus they are indirect probes of the effects on the symmetry energy. In the following, we discuss examples of such observables to demonstrate the possibilities and challenges to determine the density dependence of the symmetry energy in HICs.

3.2. Collective Flow

The flow of nuclear matter out of the interaction region indicates compression. The flow can be characterized by a kinetic momentum tensor. Non-sphericity indicates dynamic effects originating from the EoS, whose orientation with respect to the beam direction represents the collective sideward or directed flow. A difference in the two minor axes indicates the existence of elliptic flow. It has become customary to express both directed and elliptic flows, as well as possible higher-flow components, by means of a Fourier decomposition of the azimuthal distributions measured with respect to the orientation of the reaction plane ϕ_R [31]:

$$\frac{dN}{d(\phi - \phi_R)} = \frac{N_0}{2\pi} \left(1 + 2 \sum_{n \geq 1} v_n \cos n(\phi - \phi_R) \right), \tag{3}$$

where N_0 is the azimuthally integrated yield. The coefficients $v_n \equiv \langle \cos n(\phi - \phi_R) \rangle$ are functions of particle type, impact parameter, rapidity y, and the transverse momentum p_t; v_1 and v_2 are the directed and elliptic flows, respectively.

Directed flow indicates the repulsion or attraction of the colliding nuclei and thus the deflection in the reaction plane. It originates from the compressional properties of the EoS, but also from the momentum dependence of the potential, particularly at higher incident energies. Thus it may also reverse its sign at higher energies, such as is shown, for example, by Ivanov [32]. The elliptic flow describes the squeeze-out of the participant matter perpendicular to the reaction plane and is thus very directly connected to compression. It is a promising probe of the stiffness of the EoS and has been investigated in detail in symmetric and asymmetric nuclear matter.

An excitation function of the elliptic flow of $Z = 1$ particles in ^{197}Au+^{197}Au collisions compiled from various experiments [33] is shown in Figure 4. At lower energies, the collective angular

momentum in the mean-field-dominated dynamics causes the observed in-plane enhancement of emitted reaction products; that is, $v_2 > 0$. Squeeze-out perpendicular to the reaction plane, that is, $v_2 < 0$, as a result of shadowing by the spectator remnants is observed at incident energies between about 150 and 4 GeV/nucleon with a maximum near 400 MeV/nucleon. Thus elliptic flow at these energies is particularly sensitive to the compression energy and thus to the EoS. The figure also shows that elliptic flow can be measured quite precisely, as demonstrated by the good agreement of data sets from different experiments in the overlap regions of the studied intervals in collision energy [33–35].

To determine the high-density symmetry energy, the neutron–proton differential measurement of elliptic flow is particularly promising [36]. It involves the more difficult measurement of neutron flow. Such measurements have been performed recently by the ASY-EOS collaboration at the Gesellschaft für Schwerionenforschung (GSI) in Darmstadt, Germany [37], and a result of this experiment and the analysis using a QMD code is shown in Figure 5. Here the flow ratio of neutrons over all charged particles is shown as a function of the transverse momentum per nucleon. The data are compared to two predictions using the same momentum-dependent isoscalar field and two versions of the symmetry energy, characterized by an exponent γ of a polynomial parametrization of the symmetry energy $E_{sym}^{pot} = C(\rho/\rho_0)^\gamma$, $C \approx 12$ MeV. A best fit yielded a γ value of around 0.75, which represents a somewhat soft symmetry energy. It was also shown that the sensitivity of the experiment to density was in the range of 1–2 ρ_0; that is, it tests densities higher than saturation density. This, together with a previous experiment [38] with lower sensitivity, was a first direct determination of the symmetry energy above saturation density. Experiments at the facility NICA at the Joint Institute for Nuclear Reactions at Dubna, Russia or the Facility for Anti-proton and Ion Research (FAIR) at Darmstadt, Germany, should be able to probe even higher densities and explore the region of the deconfinement phase transition.
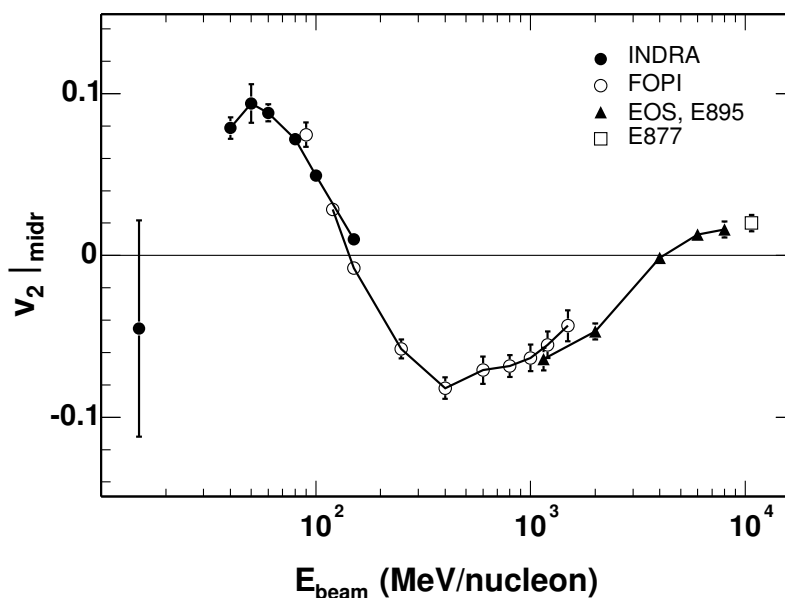

Figure 4. Elliptic flow parameter v_2 at midrapidity for ^{197}Au+^{197}Au collisions at intermediate impact parameters ($\approx$5.5–7.5 fm) as a function of incident energy. The filled and open circles represent the INDRA and FOPI data for $Z = 1$ particles, the triangles represent the equation-of-state (EoS) and E895 data for protons, and the squares represent the E877 data for all charged particles. Figure taken from [33] with permission, where the references to the data are also given.
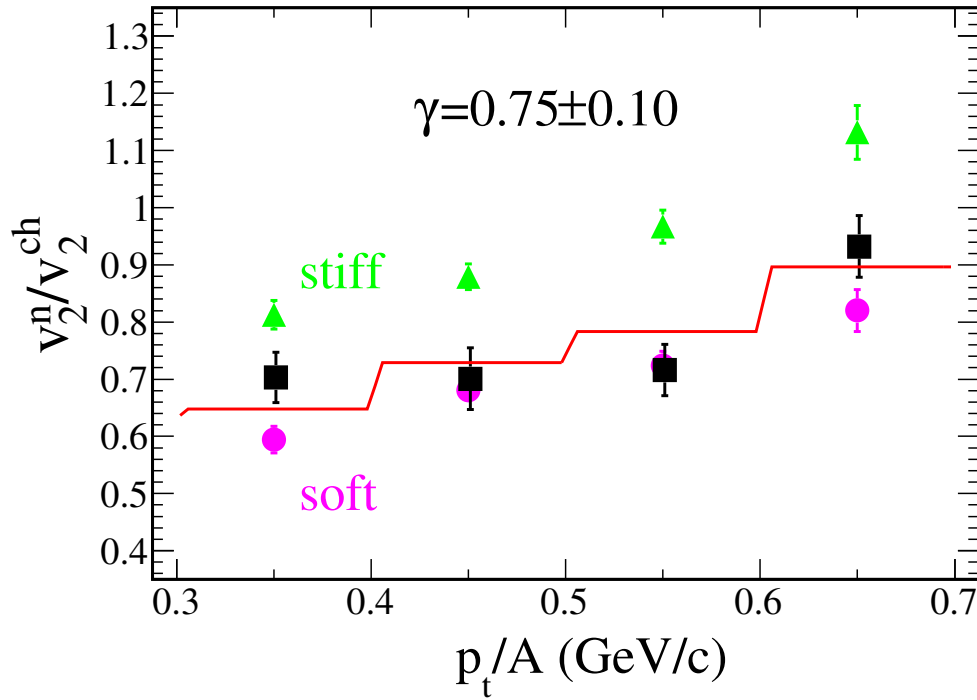
Figure 5. Elliptic flow ratio of neutrons over all charged particles for central ($b < 7.5$ fm) collisions of ^{197}Au+^{197}Au at 400 MeV/nucleon as a function of the transverse momentum per nucleon p_t/A. The black squares represent the experimental data; the green triangles and purple circles represent the QMD predictions for stiff ($\gamma = 1.5$) and soft ($\gamma = 0.5$) power-law exponents of the potential term, respectively. The solid line is the result of a linear interpolation between the predictions, weighted according to the experimental errors of the included four bins in p_t/A and leading to the indicated $\gamma = 0.75 \pm 0.10$. Figure taken from [37].

3.3. Light Cluster Emission

Pre-equilibrium nucleons and light clusters are emitted early in energetic collisions and are distinguished from equilibrium evaporation particles by their higher energies. Ratios of isospin partners should be sensitive to the symmetry potential, to both the value of the potential at the relevant density and to the momentum dependence. The latter can be characterized by an effective mass as $m^*/m = (1 + (m/\hbar^2 k)\partial U/\partial k)^{-1}$. The momentum dependence of the isospin-dependent potential U_τ, $\tau = \{n, p\}$, then leads to an isospin splitting of the effective masses for neutrons and protons. The effect of these properties of the isospin potential can be seen in Figure 6, where for a collision $^{136}Xe + ^{124}Sn$ at 150 AMeV, the (single) yield ratio of neutrons over protons, $R(n/p; {}^{136}Xe + {}^{124}Sn)$, is shown as a function of the transverse energy [39]. The calculations are shown for four combinations of the density dependence (soft vs. stiff) and the effective masses ($m_n^* > m_p^*$ vs. $m_n^* < m_p^*$). For lower transverse energies of the emitted particles, the density dependence of the symmetry energy is dominant, and the soft case has the larger repulsion for neutrons below ρ_0, while for higher transverse energies, the momentum dependence dominates and the lighter effective masses are emitted more readily. This behavior opens the possibility to separate the density and momentum dependence of the symmetry energy. At higher incident energies, the momentum dependence dominates increasingly more [40]. Similar behavior is seen for isospin partners of light clusters, such as $t/^3He$ in the right panel of Figure 6.

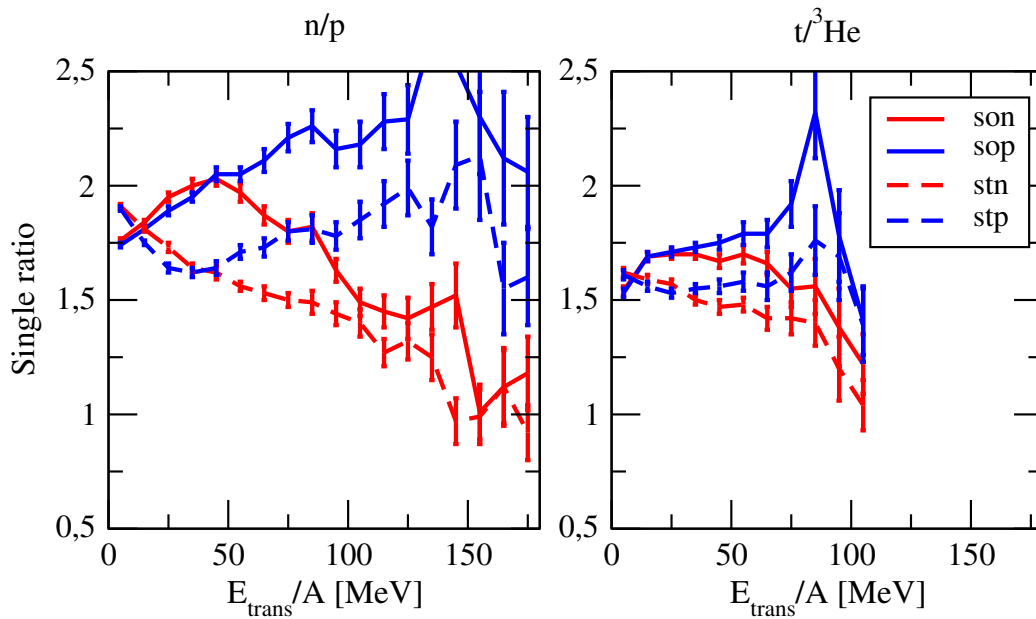**Figure 6.** (**Left**) The neutron–proton ratio in $^{136}Xe +^{124}Sn$ collisions at 150 AMeV for different choices of the symmetry energy and ordering of the effective masses, as indicated in the legend and discussed in the text: solid and dashed lines for stiff and soft symmetry energies, respectively, and red and blue lines for $m_n^* > m_p^*$ and $m_n^* < m_p^*$, respectively. Thus the labels *son* and *sop* indicate soft symmetry energy with $m_n^* > m_p^*$ and $m_n^* < m_p^*$, respectively, and the labels *stn* and *stp* are analogous for stiff symmetry energy. (**Right**) The corresponding tritium over ^3He ratio. Figure taken from [41].

In Figure 7, the n/p emission is compared to data from Michigan State University (MSU) for Sn+Sn collisions [42]. Here, not the single ratio of neutrons over protons is compared, as in Figure 6, but the ratios of the ratios for two reactions, the double ratios (DRs):

$$\text{DR}(n/p;^{124}Sn;^{112}Sn) = \frac{\text{R}(n/p;^{124}Sn +^{124}Sn)}{\text{R}(n/p;^{112}Sn +^{112}Sn)},\qquad(4)$$

where experimental differences in the efficiency of neutron and proton detection are expected to cancel out. Shown are the "coalescence-invariant" DRs, for which neutrons and protons of all experimentally measured clusters with $A \leq 4$ are included into the coalescence-invariant cross-sections. On the other hand, the DRs for only the free protons and neutrons show little similarity to the DRs in BUU calculations [42]. This is caused by the difficulty to describe light cluster formation in transport calculations, which depends sensitively on dynamical few-body correlations that are not accounted for in the usual BUU and only classically accounted for in QMD calculations. The experimental coalescence-invariant DRs are compared to calculations in Figure 7 with two Skyrme-type density functionals, which have a very similar stiffness of the symmetry energy of $L \approx 60$ MeV but different orderings of the effective masses. The SLy4 EoS with $m_n^* < m_p^*$ seems to fit the data somewhat better, but better data are needed for the higher-energy part of the spectrum.

Light cluster emission is of interest at both lower energies and densities in the Fermi energy regime and at higher energies and densities in the range of the NICa experiments. In the first case, it was used to investigate the symmetry energy of nuclear matter at very low densities, which exists in the expansion phase of a central low-energy reaction [43]. The ratio of cluster yields between two reactions of different isospin gave information about the change in the chemical potentials and thus about the symmetry energy via isoscaling [44,45]. At the same time, the cluster ratios gave information on the density of about 0.1–0.001 ρ_0 and temperatures of a few MeV [46]. The formation of light clusters in low-density warm matter was also confirmed by quantum statistical calculations, which take into account the medium dependence of the clusters and their eventual dissolution with

increasing density [47]. Because the formation of clusters is favored by their binding energy relative to a homogeneous medium of free nucleons, the symmetry energy remains finite as the density approaches zero. The range of densities and temperatures in such investigations is also in the range of conditions in the neutrino-sphere of core-collapse supernovae and thus gives a connection between HICs and astrophysics.
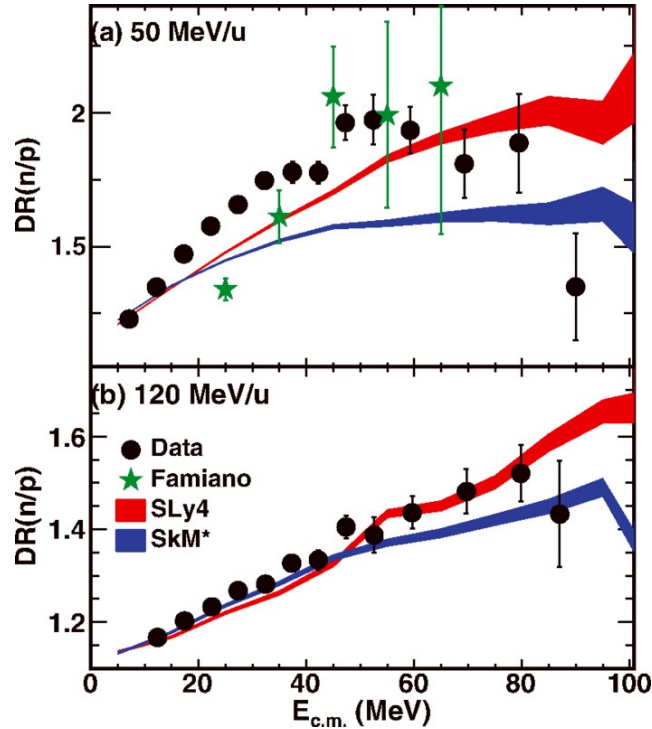

Figure 7. (Color on-line) Double ratios (DRs) of neutron over proton yields in reactions of $^{124}Sn + ^{124}Sn$ over $^{112}Sn + ^{112}Sn$ at energies of 50 and 120 AMeV as a function of the center-of-mass energy of the emitted particles. The experimental data represent coalescence-invariant cross-sections, for which neutrons and protons of all experimentally measured clusters with $A \leq 4$ are included. The calculations are Boltzmann–Uehling–Uhlenbeck (BUU) calculations with the two Skyrme-like functionals SKM and SLy4, which have a different ordering of the neutron and proton effective masses but are otherwise very similar; see text. The figure is taken from [42] with permission.

Cluster emission could also be an interesting probe for the EoS at the high densities reached in ultrarelativistic HICs, such as in NICa experiments. As discussed in [48,49], clusters may exist and survive in HICs near the deconfinement phase transition, and their flow can be used as a probe of the phase transition. Thus cluster formation in HICs is both an important probe and at the same time a challenge to transport descriptions.

3.4. Particle Production

The n/p asymmetry of the compressed system also determines the ratio of newly produced particles, which thus can serve as indicators of the symmetry energy in the high-density phase. Pions are produced predominantly via the Δ resonances $NN \rightarrow N\Delta$ and the subsequent decay $\Delta \rightarrow N\pi$. The ratio of the isospin partners π^-/π^+ can thus serve as a probe of the high-density symmetry energy. As analyzed in [50], there are competing effects on the Δ and pion production from the isospin-dependent mean fields and the Δ production threshold conditions.

The results from recent theoretical analyses of the π^-/π^+ ratio using different models of symmetry energies and different program codes are collected in the right panel of Figure 8, while the corresponding symmetry energy density dependencies are shown in the left panel [51–54].

These are compared to the data of the Four-PI collaboration (FOPI) [55]. For each model, the results for two parameter sets of different stiffness are shown (stiffer: blue; softer: red). As is seen, the results of the different models are very different not only quantitatively; even the trend with the stiffness of the symmetry energy is not consistent. A reason may lie in different modeling of the $\Delta - \pi$ dynamics, as well as in the competing mean-field and threshold effects, for which slightly different treatments might lead to large differences [50]. The code comparison of pion production, mentioned above, should further serve to aid the understanding of these discrepancies. This issue needs clarification in view of the sensitivity of the pion observables and the data situation. More information should be gained by discussing not the energy-integrated yield ratios but the spectral behavior of the ratio, as different energy pions are expected to probe different stages of the evolution of the reaction [56].
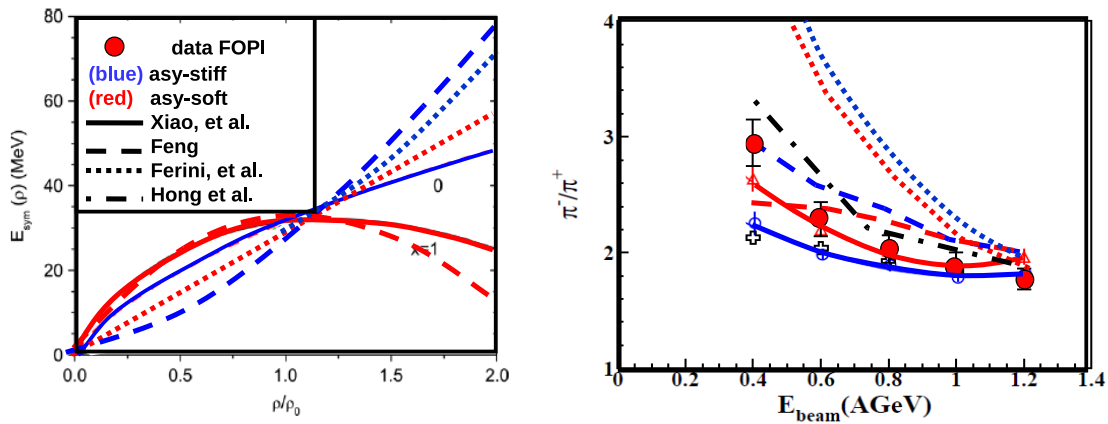

Figure 8. (**Right**) The π^-/π^+ ratio in $Au + Au$ collisions as a function of incident energy as measured by the FOPI collaboration and calculated by different groups, as indicated in the legend of the left panel and discussed in the text. The blue and red lines refer to the softer and stiffer symmetry energies, respectively, used in the different models, which are identified by the signature of the line. (**Left**) This panel shows the density dependence of the symmetry energy used in the models. Figure taken from [41].

It has also been suggested that the ratio of the anti-strange kaon isospin partners, K^0/K^+, could be a useful observable for the symmetry energy [57]. Indeed, kaon production has been one of the most useful observables to determine the EoS of symmetric nuclear matter [29]. The anti-strange kaons weakly interact with nuclear matter and are thus a direct probe of the dense matter in which they are produced. Theoretical analyses show a similar, if not greater, sensitivity to the symmetry energy compared to pion ratios.

4. Discussion and Summary

Constraints for the density dependence of the nuclear symmetry energy determined from HICs are shown in the left panel of Figure 9 for the range of densities presently explored, which also includes some results from nuclear-structure studies. We briefly discuss the various constraints shown in the figure. At very low densities, the symmetry energy was determined from the light cluster yields of the decay of the participant in low-energy HICs (solid triangles) [46], as discussed in Section 3.3. The very precise description of masses of nuclei by energy density functionals constrained the symmetry energy around saturation density—in fact about 40% below—because of the surface contribution, as is shown in the figure (solid circle and square) [3]. The analysis of the shift of the isobaric analog resonances (IAS) yielded rather stringent constraints on the asymmetry density in nuclei (dotted contour) [58]. Transport analysis of HICs, mainly of Sn+Sn but also other systems, at energies from 50 to about 200 AMeV probed the symmetry energy below saturation density from observations of isospin transport between the residual fragments (gray contour) [30]. The constraints from n/p flow ratios at the relativistic energies discussed in Section 3.2 [37] are shown

by the red area (as well as the yellow area from an earlier measurement with smaller precision [38]) in the density region of 1.5–2 ρ_0, where they were the most sensitive. One result of the analysis of the π^-/π^+ ratio is shown by the blue line [51], which is also shown in Figure 8. As discussed there, this result is controversial and in any case was in conflict with the result of the flow measurements.
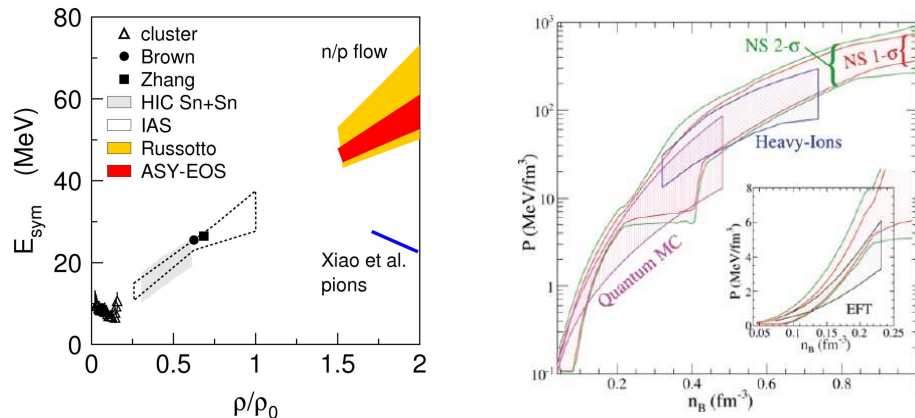

Figure 9. (**Left panel**) Constraints deduced for the density dependence of the zero-temperature symmetry energy from the ASY-EOS data (red area, [37]) in comparison with the FOPI-LAND result (yellow area, [38]) as a function of the reduced density ρ/ρ_0. The low-density results of [30,58–60] as reported in [3] are given by the symbols, the gray area (heavy-ion collision—HIC), and the dashed contour (isobaric analog resonances—IAS); see also text. Figure taken from [37]. (**Right panel**) Synopsis of constraints on the equation of state (EoS) of neutron star (NS) β-stable matter from microscopic calculations (quantum Monte Carlo and effective field theory (EFT)), heavy-ion collisions, and NS observations in a pressure–density diagram. Figure taken from A. Steiner et al. [6] with permission.

The results of the density dependence on the symmetry energy from the nuclear structure and reactions were seen to converge reasonably well; the disagreements from the pion ratio observations will hopefully be clarified via the code comparison investigations discussed in Section 2.3. In the right panel of Figure 9, these results are contrasted with results from microscopic calculations; constraints from HICs, in this case from [1]; and constraints from NS observations. The microscopic calculations were performed with chiral effective field theory (EFT) using various many-body techniques [61,62]. The NS constraints originate from mass–radius studies and from the maximum mass of observed NSs [5,6], but constraints from NS mergers are not yet given. It is seen that overall, the results tended to converge, but a reduction in the uncertainties from all sources, many-body calculations, structure, reactions, and astrophysics is expected in the future.

References

1. Danielewicz, P.; Lacey, R.; Lynch, W.G. Determination of the equation of state of dense matter. *Science* **2002**, *298*, 1592.
2. Li, B.A.; Ramos, À.; Verde, G.; Vidaña, I. Topical Issue on the Nuclear Symmetry Energy. *Eur. Phys. J. A* **2014**, *50*, 1–3.
3. Horowitz, C.J.; Brown, E.F.; Kim, Y.; Lynch, W.G.; Michaels, R.; Ono, A.; Piekarewicz, J.; Tsang, M.B.; Wolter, H.H. A way forward in the study of the symmetry energy: experiment, theory, and observation. *J. Phys. G* **2014**, *41*, 093001.

4. Demorest, P.D.; Pennucci, T.; Ransom, S.M.; Roberts, M.S.E.; Hessels, J.W.T. A two-solar-mass neutron star measured using Shapiro delay. *Nature* **2010**, *467*, 1081–1083 .

5. Steiner, A.W.; Lattimer, J.M.; Brown, E.F. The equation of etate from observed masses and radii of neutron stars. *Astrophys. J.* **2010**, *722*, 33.

6. Steiner, A.W.; Lattimer, J.M.; Brown, E.F. The neutron star mass-radius relation and the equation of state of dense matter. *Astrophys. J. Lett.* **2013**, *765*, L5.

7. Abott, P.B.; Abbott, R.; Abbott, T.D.; Acernese, F.; Ackley, K.; Adams, C.; Adams, T.; Addesso, P.; Adhikari, R.X.; Adya, B.; et al. GW170817: Implications for the stochastic gravitational-wave background from compact binary coalescences. *Phys. Rev. Lett.* **2017**, *119*, 161101.

8. Goldstein, A.; Veres, P.; Burns, E.; Briggs, M.S.; Hamburg, R.; Kocevski, D.K.; Wilson-Hodge, C.A.; Preece, R.D.; Poolakkil, S.; Roberts, O.J.; et al. An ordinary short gamma-ray burst with extraordinary implications: Fermi-GBM detection of GRB 170817A. *Astrophys. J. Lett.* **2017**, *848*, L14.

9. Savchenko, V.; Ferrigno, C.; Kuulkers, E. INTEGRAL detection of the first prompt gamma-ray signal coincident with the gravitational-wave event GW170817. *Astrophys. J. Lett.* **2017**, *848*, L15.

10. Hinderer, T. Tidal LOVE numbers of neutron stars. *Astrophys. J.* **2008**, *677*, 1216.

11. Fattoyev, F.J.; Piekarewicz, J.; Horowitz, C.J. Neutron skins and neutron stars in the multimessenger era. *Phys. Rev. Lett.* **2018**, *120*, 172702.

12. Krastev, P.G.; Li, B.A. Imprints of the nuclear symmetry energy on the tidal deformability of neutron stars. *arXiv* **2018**, arXiv:1801.04620.

13. Bauswein, A.; Just, O.; Janka, H.-T.; Stergioulas, N. Neutron-star radius constraints from GW170817 and future detections. *Astrophys. J. Lett.* **2017**, *850*, L34.

14. Paschalides, V.; Yagi, K.; Alvarez-Castillo, D.; Blaschke, D.; Sedrakian, A. Implications from GW170817 and I-Love-Q relations for relativistic hybrid stars. *Phys. Rev. D* **2018**, *97*, 084038.

15. Danielewicz, P . Quantum theory of nonequilibrium processes I. *Ann. of Phys.* **1984**, *152*, 239–304.

16. Botermans, W.; Malfliet, R. Quantum transport theory of nuclear matter. *Phys. Rep.* **1990**, *198*, 115–194.

17. Hofmann, F.; Keil, C.M.; Lenske, H. Density dependent hadron field theory for asymmetric nuclear matter and exotic nuclei. *Phys. Rev. C* **2001**, *64*, 034314.

18. Fuchs, C.; Lenske, H. Rearrangement in the density-dependent field theory of relativistic nuclei. *Phys. Lett. B* **1995**, *345*, 355.

19. Fuchs, C.; Lenske, H.; Wolter, H.H. Density dependent hadron field theory. *Phys. Rev. C.* **1995**, *52*, 3043.

20. Ono, A.; Horiuchi, H.; Maruyama, T.; Ohnishi, A. Antisymmetrized version of molecular dynamics with two-nucleon collisions and its application to heavy ion reactions. *Prog. Theor. Phys.* **1992**, *87*, 1185.

21. Bertsch, G.F.; Gupta, S.D. A guide to microscopic models for intermediate energy heavy ion collisions. *Phys. Rep.* **1988**, *160*, 189.

22. Aichelin, J. Quantum molecular dynamics: A dynamical microscopic n-body approach to investigate fragment formation and the nuclear equation of state in heavy ion collisions. *Phys. Rep.* **1991**, *202*, 233–360.

23. Napolitani, P.; Colonna, M. Bifurcations in Boltzmann—Langevin one body dynamics for fermionic systems. *Phys. Lett. B* **2013**, *726*, 382–386.

24. Napolitani, P.; Colonna, M. Frustrated fragmentation and re-aggregation in nuclei: A non-equilibrium description in spallation. *Phys. Rev. C* **2015**, *92*, 034607.

25. Colonna, M.; di Toro, M.; Guarnera, A.; Maccarone, S.; Zielinska-Pfabé, M.; Wolter, H.H. Fluctuations and dynamical instabilities in heavy-ion reactions. *Nucl. Phys. A* **1998**, *642*, 449–460.

26. Colonna, M. Fluctuations and Symmetry Energy in Nuclear Fragmentation Dynamics. *Phys. Rev. Lett.* **2013**, *110*, 042701.

27. Xu, J.; Chen, L.-W.; Tsang, M.B.; Wolter, H.H.; Zhang, Y.-X.; Aichelin, J.; Colonna, M.; Cozma, D.; Danielewicz, P.; Feng, Z.-Q.; et al. Understanding transport simulations of heavy-ion collisions at 100 A and 400 A MeV: Comparison of heavy-ion transport codes under controlled conditions. *Phys. Rev. C* **2016**, *93*, 044609.

28. Zhang, Y.-X.; Wang, Y.-J.; Colonna, M.; Danielewicz, P.; Ono, A.; Tsang, M.B.; Wolter, H.H.; Xu, J.; Chen, L.-W.; Cozma, D.; et al. Comparison of heavy-ion transport simulations: Collision integral in a box. *Phys. Rev. C.* **2018**, *97*, 034625.

29. Fuchs, C.; Faessler, A.; Zabrodin, E.; Zheng, Y.-M. Probing the nuclear equation of state by K^+ production in heavy-ion collisions. *Phys. Rev. Lett.* **2001**, *86*, 1974.

30. Tsang, M.B.; Stone, J.R.; Camera, F.; Danielewicz, P.; Gandolfi, S.; Hebeler, K.; Horowitz, C.J.; Lee, J.; Lynch, W.G.; Kohley, Z. et al. Constraints on the symmetry energy and neutron skins from experiments and theory. *Phys. Rev. C* **2012**, *86*, 015803.

31. Poskanzer, A.M.; Voloshin, S.A. Methods for analyzing anisotropic flow in relativistic nuclear collisions. *Phys. Rev. C* **1998**, *58*, 1671.

32. Ivanov, Y.B. Directed flow in heavy-ion collisions and its implications for astrophysics. *Universe* **2017**, *3*, 79.

33. Andronic, A.; Łukasik, J.; Reisdorf, W.; Trautmann, W. Systematics of stopping and flow in Au + Au collisions. *Eur. Phys. J. A* **2006**, *30*, 31–46.

34. Reisdorf, W.; Leifels, Y.; Andronic, A.; Averbeck, R. Barret, V. Systematics of azimuthal asymmetries in heavy ion collisions in the 1A GeV regime. *Nucl. Phys. A* **2012**, *876*, 1–60.

35. Łukasik, J.; Auger, G.; Bellaize, M.L.; Be, N.; Bittiger, R.; Bocage, F.; Borderie, B.; Bougault, R.; Bouriquet, F.; Charvet, J.L.; Chbihi, A.; et al. Directed and elliptic flow in ^{197}Au+^{197}Au at intermediate energies. *Phys. Lett. B* **2005**, *608*, 223–230.

36. Trautmann, W.; Wolter, H.H. Elliptic flow and the symmetry energy at supra-saturation density. *Int. J. Mod. Phys. E* **2012**, *21*, 1230003.

37. Russotto, P.; Gannon, S.; Kupny, S.; Lasko, P.; Acosta, L.; Adamczyk, M.; Al-Ajlan, A.; Amorini, F. Results of the ASY-EOS experiment at GSI: The symmetry energy at suprasaturation density. *Phys. Rev. C* **2016**, *94*, 034608.

38. Russotto, P.; Wu, P.Z.; Zoric, M.; Chartier, M.; Leifels, Y.; Lemmon, R.C.; Li, Q.; Łukasik, J.; Pagano, A.; Pawłowski, P.; et al. Symmetry energy from elliptic flow in ^{197}Au + ^{197}Au. *Phys. Lett. B* **2011**, *697*, 471–476.

39. Wolter, H.H.; Zielinska-Pfabe, M.; Decowski, P.; Colonna, M.; Bougault, R.; Chbihi, A. Symmetry energy dependence of light fragment production in heavy ion collisions. *EPJ Web Conf.* **2014**, *66*, 03097.

40. Giordano, V.; Colonna, M.; di Toro, M.; Greco, V.; Rizzo, J. Isospin emission and flow at high baryon density: A test of the symmetry potential. *Phys. Rev. C* **2010**, *81*, 064611.

41. Wolter, H.H. The nuclear symmetry energy in heavy ion collisions. *Phys. Part. Nucl.* **2015**, *46*, 781.

42. Coupland, D.D.S.; Youngs, M.; Chajecki, Z.; Lynch, W.G.; Tsang, M.B.; Zhang, Y.X.; Famiano, A.; Ghosh, T.K.; Giacherio, B.; Kilburn, M.A.; et al. Probing effective nucleon masses with heavy-ion collisions. *Phys. Rev. C* **2016**, *94*, 011601.

43. Kowalski, S.; Natowitz, J.B.; Shlomo, S.; Wada, R.; Hagel, K.; Wang, J.; Materna, T.; Chen, Z.; Ma, Y.G.; Qin, L.; et al. Experimental determination of the symmetry energy of a-low density nuclear gas. *Phys. Rev. C* **2007**, *75*, 014601.

44. Tsang, M.B.; Friedman, W.A.; Gelbke, C.K.; Lynch, W.G.; Verde, G.; Xu, H.S. Isotopic scaling in nuclear reactions. *Phys. Rev. Lett.* **2001**, *86*, 5023.

45. Tsang, M.B.; Friedman, W.A.; Gelbke, C.K.; Lynch, W.G.; Verde, G.; Xu, H.S. Conditions for isoscaling in nuclear reactions. *Phys. Rev. C* **2001**, *64*, 041603.

46. Natowitz, J.B.; Röpke, G.; Typel, S.; Blaschke, D.; Bonasera, A.; Hagel, K.; Klähn, T.; Kowalski, S.; Qin, L.; Shlomo, S.; Wada, R.; Wolter, H.H. Symmetry energy of dilute warm nuclear matter. *Phys. Rev. Lett.* **2010**, *104*, 202501.

47. Typel, S.; Röpke, G.; Klähn, T.; Blaschke, D.; Wolter, H.H. Composition and thermodynamics of nuclear matter with light clusters. *Phys. Rev. C* **2010**, *81*, 015803.

48. Bastian, N.-U.; Batyuk, P.; Blaschke, D.; Danielewicz, P.; Yu, B. Light cluster production at NICA. *Eur. Phys. J. A* **2016**, *52*, 244.

49. Röpke, G.; Blaschke, D.; Ivanov, Y.B.; Karpenko, I.; Rogachevsky, O.V.; Wolter, H.H. Medium effects on freeze-out of light clusters at NICA energies. *Phys. Part. Nucl. Lett.* **2018**, *15*, 225.

50. Ferini, G.; Colonna, M.; Gaitanos, T.; di Toro, M. Aspects of particle production in isospin-asymmetric matter. *Nucl. Phys. A* **2005**, *762*, 147–166.

51. Xiao, Z.; Li, B.A.; Chen, L.W.; Yong, G.C.; Zhang, M. Circumstantial evidence for a soft nuclear symmetry energy at suprasaturation densities. *Phys. Rev. Lett.* **2009**, *102*, 062502.

52. Prassa, V.; Ferini, G.; Gaitanos, T.; Wolter, H.H.; Lalazissis, G.; di Toro, M. In-medium effects on particle production in heavy ion collisions. *Nucl. Phys. A* **2007**, *789*, 311–333.

53. Feng, Z.Q.; Jin, G.M. Probing high-density behavior of symmetry energy from pion emission in heavy-ion collisions. *Phys. Lett. B* **2010**, *683*, 140–144.

54.　Hong, J.; Danielewicz, P. Subthreshold pion production within a transport description of central Au + Au collisions. *Phys. Rev. C* **2014**, *90*, 024605.

55.　Reisdorf, W. The FOPI Collaboration. Systematics of pion emission in heavy ion collisions in the 1 A GeV regime. *Nucl. Phys. A* **2007**, *781*, 459–508.

56.　Tsang, M.B. *Pion Production in Rare-Isotope Collisions*; Nuclear Symmetry Energy 2017 (NuSYM2017); Grand Accélérateur National D'Ions Lourds: Caen, France, 2017.

57.　Ferini, G.; Gaitanos, T.; Colonna, M.; di Toro, M.; Wolter, H.H. Isospin effects on subthreshold kaon production at intermediate energies. *Phys. Rev. Lett.* **2006**, *97*, 202301.

58.　Danielewicz, P.; Lee, J. Symmetry energy II: Isobaric analog states. *Nucl. Phys. A* **2014**, *922*, 1–70.

59.　Brown, B.A. Constraints on the Skyrme Equations of State from Properties of Doubly Magic Nuclei. *Phys. Rev. Lett.* **2013**, *111*, 232502.

60.　Zhang, Z.; Chen, L.-W. Constraining the symmetry energy at subsaturation densities using isotope binding energy difference and neutron skin thickness. *Phys. Lett. B* **2013**, *726*, 234–238.

61.　Zhang, Z.; Chen, L.-W.; Pethick, C.J.; Schwenk, A. Constraints on neutron star radii based on chiral effective field theory interactions. *Phys. Rev. Lett.* **2010**, *105*, 161102.

62.　Gandolfi, S.; Carlson, J.; Reddy, S. Maximum mass and radius of neutron stars, and the nuclear symmetry energy. *Phys. Rev. C* **2012**, *85*, 032801.